BNL-219945-2020-JAAM

Synchrotron Operando Depth Profiling Studies of State-of-Charge Gradients in Thick Li(Ni0.8Mn0.1Co0.1)O-2 Cathode Films

Z. Li, P. G. Khalifah

To be published in "CHEMISTRY OF MATERIALS"

August 2020

Chemistry Department

Brookhaven National Laboratory

U.S. Department of Energy

USDOE Office of Energy Efficiency and Renewable Energy (EERE), Vehicle Technologies Office (EE-3V)

DISCLAIMER

Synchrotron Operando Depth Profiling Studies of State-of-Charge Gradients in Thick $Li(Ni_{0.8}Mn_{0.1}Co_{0.1})O_2$ Cathode Films

Zhuo Li, Liang Yin, Gerard S. Mattei, Monty R. Cosby, Byoung-Sun Lee, Zhaohui Wu, Seong-Min Bak, Karena W. Chapman, Xiao-Qing Yang, Ping Liu, and Peter G. Khalifah*

ABSTRACT: Higher energy densities in rechargeable batteries can be achieved using thicker cathode films, though it is a challenging endeavor since the electrochemical performance of thick electrodes is substantially worse than that of the conventional thin electrodes due to a variety of transport limitations, which are thus far poorly understood. Operando synchrotron studies have been, for the first time, applied to thick film samples to determine the depth-dependent state of charge (SOC) distribution inside 170 micron thick $Li(Ni_{0.8}Mn_{0.1}Co_{0.1})O_2$ cathode films using an unconventional radial diffraction experiment geometry, allowing the SOC to be probed with both high spatial resolution (20 microns) and high temporal resolution (hundreds of time steps) in a single experiment. The resulting data allow the evolution of vertical inhomogeneity within these thick cathode films to be determined during cycling and they reveal a number of unexpected phenomena, such as the continuation of charging at some heights within the cathode during the discharge cycle of the cell. The new availability of comprehensive depth-dependent SOC data will drive the parameterization and advancement of whole-cell models, leading to an improved understanding of large-scale transport phenomena and enhanced capabilities for the rational design of thick electrodes with improved performance.

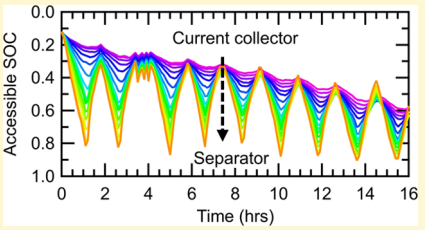

In modern society, batteries are a nearly ubiquitous technology for energy storage and are found within a multitude of high-tech applications.[1−5] Presently, the necessity to develop batteries with higher energy densities is being most strongly driven by the needs of the automotive industry, where vehicular range is a key consumer metrics.[6−8] While the performance of a battery depends strongly on the specific chemical redox processes supported by the active material (both at the cathode and the anode), the full expected capacity of these electrodes will not be realized unless the overall battery device is designed to avoid performance limitations associated with potential bottlenecks in the transport of electrons and ions within these devices.[9]

Experiments investigating changes in the cathode material during electrochemical cycling are typically designed so that the battery cathodes operate in a homogenous manner throughout their volume using a thin cathode film (typically less than 50 microns thick) together with a higher capacity anode (n/p ratio > 1) and excess electrolyte. In order to meet the industrial targets for energy density, it is necessary to be able to fabricate and efficiently operate thick battery films whose anticipated thicknesses (100−250 microns) may exceed those of typical laboratory test cells by an order of magnitude.[7] In such thick films, it is virtually guaranteed that there will be depth-dependent inhomogeneity when cells are cycled at practical rates.[10,11] In order to achieve maximal performance from thick films, it is critical to be able to quantify and model the vertical inhomogeneity, as this will allow the aspects of the cell that are mostly responsible for the inhomogeneity to be identified and mitigated.

Conventional electrochemical techniques for evaluating cells are poorly suited for understanding this inhomogeneity as they lack spatial sensitivity. While this limitation can nominally be addressed through the use of computational models,[12,13] in practice, the large number of model parameters, whose values are uncertain or are strongly dependent on the cell state of charge (e.g., electronic and ionic conductivity of the cathode), makes it implausible to validate models based only on simple electrochemical responses of cells. Similarly, conventional operando X-ray diffraction methods[14−18] that are routinely used in the battery field are unable to probe the vertical inhomogeneity since a beam traveling perpendicular to the film surface will simultaneously sample powders at all heights within the film, thus convoluting their signals.

Very recently, a promising new approach for operando diffraction experiments has been demonstrated that utilizes a radial geometry in which a narrow beam (~20 μm) aligned parallel to the plane of the sample is scanned across its vertical height (~200 μm).[19,20] This method was shown to be sensitive

to the vertical inhomogeneity in thick pellets. However, these thick pellets were typically fabricated with a low mass fraction of active material (60%) and large amounts of conductive carbon (20%) and binder (20%) and thus substantially differ from the standard commercial cast-film batteries, for which it has been shown that active material loadings exceeding 95% are achievable, providing a pathway toward overall cell energy densities of 500 Wh/kg or higher.[7,21,22] In our work, radial depth profiling methods are for the first time adapted to study industrially relevant cast films rather than pellet samples formulated to simplify operando experiments. Experimental approaches for overcoming the challenges of studying films in the thin-film geometry are described. It is shown that these thick films can be probed with good spatial and temporal sensitivity, and when the data are analyzed, a variety of unexpected phenomena that give insights into the likely origin of the inhomogeneous behavior are observed.

EXPERIMENTAL SECTION

NMC811/Li batteries were prepared for operando studies. Commercial $LiNi_{0.8}Co_{0.1}Mn_{0.1}O_2$ particles (NCM811, Ecopro) were used as the cathode-active material. Carbon black (Super C65, TIMCAL) and poly(vinylidene fluoride-hexafluoropropylene) (PVDF-HFP, Kynar Flex 2801) were used as the conducting agent and binder, respectively. A binder solution with a 10 wt % concentration was prepared by dissolving PVDF-HFP in *n*-methyl-2-pyrrolidone (NMP, Sigma-Aldrich). NCM811 and carbon black were mixed in a ratio of 90:5 (by weight) for 15 min using an agate mortar and pestle. The binder solution and additional NMP were then added to this powdered mixture to form the cathode slurry in a 90:5:5 weight ratio of NCM811: carbon black: PVDF-HFP. The slurry was milled overnight with ZrO_2 balls at a 1:1 ball-to-powder weight ratio. The slurry was then cast on an Al foil using the doctor blade method with the active material loading controlled to be 50−60 mg/cm^2 for these electrodes, which were then dried in a vacuum oven at 120 °C. The electrodes were then punched into 15 mm diameter disks and calendared to have a porosity of 20%, resulting in a thickness of 170 microns as measured using a micrometer and a calculated density of 3.27 g/cm^3. For operando studies, an electrolyte of $LiPF_6$ (1.0 M, BASF) in ethylene carbonate (EC, BASF) and dimethyl carbonate (DMC, BASF) in a ratio of 1:1 by weight was prepared in an argon-filled glovebox. The cell anode was a 250 μm thick lithium metal foil (MTI). Glass fiber (1 micron pore size, Whatman GF/B) was used as the separator; its thickness was measured to be 0.68 mm prior to use.

Operando diffraction studies were carried out in a custom cell design inspired by the previously reported RATIX cell.[19] The cell body was cut from a solid Teflon (PTFE) rod with a diameter of (3/8″, 9.5 mm) and a drilled bore of 1/4″ diameter. Near the sample position, the wall thickness was reduced by milling to 10 to 15 mil over a height of about 3 mm. Stainless steel cylindrical pills (1/4” dia.) were used to hold the cell level and to provide electrical contact to the battery current collectors, with recessed O-rings on these pills used to seal the cell environment. An insulating C-clamp was constructed to hold the cell components together under constant pressure, with longer stainless steel cylinders spanning the distance between the pills and the threaded screws on the ends of the C-clamp used both to apply pressure and to electrically contact the battery cell.

The operando cells were assembled in an argon-filled glove box. One stainless steel pill was first put into a holder to support the cathode material. The NMC film was punched to obtain a 5 mm diameter disk that was placed on the pill. Next, one layer of glass fiber (1 micron pore size, Whatman) was placed on top of the cathode film, and two drops of electrolyte were added. A slightly larger diameter (7/32″, 5.6 mm) of a punched Li metal disk was placed on top of the separator and capped with another stainless steel pill. The preassembled Teflon cells were heat-sealed in a plastic pouch inside a glove box and then shipped to the Advanced Photon Source (APS) synchrotron. There, within the glove box, the sealed pouch was opened and mounted in a C-clamp holder. Three operando cells were studied in tandem during the experiment (Figure S1), with a Maccor 4300 cycler used to control the current or potential across the cells.

Synchrotron experiments were carried out at the 11-ID-B beamline of the APS using a wavelength of 0.2113 Å. The size of the beam was reduced to 20 × 250 μm (vertical × horizontal) using slits. Vertical depth profiling diffraction data were collected along the *z*-axis normal to the plane of the electrode film using a line scan of 41 vertical steps (increment of 20 microns) that was repeated every 6 min. Diffraction data were collected on a PerkinElmer amorphous silicon-based area detector (2048 × 2048 pixels with 200 μm sides) at 0.1 s subframe time and a total acquisition time of 1 s per image.

Electrochemical cycling was carried out at a voltage range of 2.8−4.4 V. One cell was cycled slowly at a rate of C/10 (calculated using a nominal cathode capacity of 200 mAh/g, corresponding to a current of 0.1793 mA and an areal current density of 1.01 mA/cm^2) using the CC−CV (constant current−constant voltage) protocol where the constant voltage was held for 2.5 h. The second cell was cycled more quickly (C/3 rate) using the galvanostatic (CC) protocol. This cell was cycled twice at the C/3 rate, three times at the 1C rate, and finally seven more times at the C/3 rate. For the last five C/3 cycles, a 6 min CV hold was added to the end of each charge and discharge step so that at least one diffraction pattern could be collected for the cell at the end of each CC step before reversing the cell polarity. The time and capacity for each cycling step are given in Tables S1 and S2.

The 2D X-ray scattering images were integrated using GSAS-II.[23] Data from a CeO_2 powder standard in a 1.1 mm diameter capillary mounted next to the cell were first used for coarse calibration (a distance of ∼947 mm). Next, finer custom distance calibration was carried out using diffraction patterns for the pristine NMC samples separately for each height using data collected within the operando cell immediately prior to cycling as an internal standard. Areas of the image were masked to exclude both the central beam stop and the detector edge (data within 20 pixels of edge), with data integrated over a 2θ range of 0.5 to 12°.

Modeling of diffraction patterns was carried out using TOPAS software (version 6, Bruker AXS). First, a single pattern at each height was refined to obtain a reasonable starting model. In addition to peaks from the main NMC phase, diffraction patterns had peaks from PTFE (from the cell wall) at all heights and peaks from Fe (from pills) and Al (from the current collector) at some heights (due to cell tilt misalignment). The PTFE contribution was dominated by a single peak observed near an angle of 2.48° (d = 4.90 Å), which was incorporated into refinements as a single peak phase. The contributions from Fe and Al were modeled as separate phases using the Pawley method. After finishing the single pattern refinements at each height, sequential refinements across all scans for a given height were subsequently run using a Python script.

For NMC, Rietveld refinements were used to determine the parameters of interest, including lattice parameters, crystallite size and strain, isotropic atomic displacement factors, site occupancies, and antisite defect concentrations. The influence of geometric aberrations due to the long beam path length through the sample and due to tilt misalignment is discussed in more detail in the Supporting Information (Figures S2−S6) and elsewhere.[24] Due to the significant cell misalignment, many diffraction patterns during cycling were observed to have two pairs of NMC peaks as a result of beam sampling both the front and the back of the cathode film while they significantly differed in their state of charge. To account for this, patterns of this type were explicitly fit using two different NMC phases differing in their state of charge. This was done for a slowly charged (C/10) cell at positions from +89 to −171 microns and for a rapidly charged (C/3) cell at positions from +106 to −114 microns. The relative scale factors of the two NMC phases were first refined using a pattern collected at the end of the first charge cycle and then fixed at this ratio for use at all times during sequential refinements. In the two-phase regions, reported parameters are the weighted average of those of the two NMC phases.

RESULTS AND DISCUSSION

Slow Cycling. Initial investigations were carried out using the cell containing the $Li(Ni_{0.8}Mn_{0.1}Co_{0.1})O_2$ cathode (denoted NMC811) cycled between 2.8 and 4.4 V (vs Li^+/Li) against Li metal at a rate of C/10 (based on a nominal capacity of 200 mAh/g) using the CC−CV protocol (constant current–constant voltage) with a CV hold time of 2.5 h. This rate corresponds to a current density of 1.0 mAh/cm^2 at the cathode. These conditions led to an experimentally accessible specific capacity of 189 mAh/g, which should produce vertical inhomogeneity within the films since it is only ∼85% of the maximum practically accessibly capacity for this system (∼220 mAh/g) and ∼ 70% of the theoretical capacity associated with full delithiation (275.5 mAh/g).

Data collection on the cell started in its pristine state without the use of any preliminary formation cycles to precondition the cell, allowing the use of known cathode lattice parameters (separately measured on a high-resolution powder diffractometer 11-BM)[25] for accurate calibration of the detector geometry. A depth profiling scan comprising 41 diffraction patterns was collected every 6 min during cycling, with the total acquisition time for each vertical scan being about 45 s (including motion) due to the short acquisition time of each pattern (1 s). The time steps for depth profiling were short relative to the time required for each charge or discharge step (60−600 min).

Each of the more than 5000 diffraction patterns were analyzed through Rietveld refinement, with some representative refinements shown in Figure S7. Due to the complex absorption behavior of the beam passing through the sample cell, the primary refined quantities of interest were the *a* and *c* lattice parameters, which could be effectively extracted at all states of charge by fitting to the initial *R*-3 *m* symmetry α-$NaFeO_2$ structure type despite the multiple subtle structural transitions that occur during cycling.[8] Representative plots of lattice parameters obtained at a beam height of z = +189 microns (relative to the sample center) are shown in Figure 1. The refined lattice parameters vary smoothly as a function of time, indicating that the measurement precision is very high relative to the magnitude of lattice parameter changes that occur during cycling.

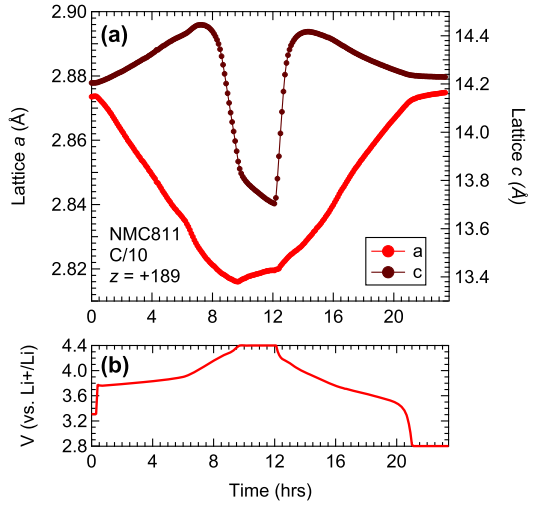

Figure 1. (a) Evolution of *a*- and c-lattice parameters during an operando scan at z = +189 microns (relative to the center of the film) that exclusively probed the front of the NMC811 electrode. (b) Voltage profile during cycling.

On charging, the *c*-lattice parameter first increases and then greatly decreases, a behavior which is fully consistent with the bulk behavior previously reported for this and other NMC compositions.[26] The behavior of the *c*-lattice parameter is essentially reversed during discharge, though it can be seen that the maximum value of this parameter is slightly lower during discharge than during the charge cycle, suggesting that there are irreversible structural changes that occur during this transformation. There is also evidence of irreversible changes in the behavior of the *a*-lattice parameter, which is observed to change nonmonotonically during charging (decreases during the CC charge up to 4.4 V but then increases during the CV hold at 4.4 V). However, during discharge, the *a*-lattice parameter changes monotonically, in contrast to the charge cycle. This behavior suggests that the different electrochemical responses observed during the first charge cycle of NMC811 compounds (often called a formation cycle) when charging to 4.4 V has an intrinsic structural origin, rather than being purely associated with interphase formation or extrinsic surface contaminants.

While the structural changes observed at z = +189 generally reflect the expected behavior of the NMC811 samples previously observed in bulk studies,[26−29] a comparison of the lattice parameter changes measured at different heights in the present depth profiling experiments indicates that other parts of the cell experience significant limitations in their ability to cycle. Comparisons of the variation in lattice parameters for the four scans collected at the front of the cathode (closest to the separator) and the four scans collected at the back of the cathode (closest to the current collector) are shown in Figure 2a,b. The front layers of the thick cathode behave nearly indistinguishably and can reach a state of charge (SOC) comparable to that which can be obtained in conventional thin-film studies. In contrast, the scans that probe the back of the cathode show a much greater degree of inhomogeneity and have lattice parameters which vary less, indicating that this portion of the thick cathode film cannot be fully charged. It can thus be concluded that transport limitations are most severe at the back of the present cell near the current collector. This strongly suggests that ionic transport limitations are mostly responsible for the reduced capacity of the thick films, as electronic limitations would result in the lowest local capacity instead being seen at the front of the cathode film.

It is possible to obtain more direct chemical insights into the depth-dependent cycling behavior than are provided by the lattice parameters alone. Although both the *a*- and *c*-lattice parameters exhibit complex, nonmonotonic behavior during cycling, the overall unit cell volume behaves in a much simpler manner since the removal of ions from the solid-state lattice typically results in a linear change in the unit cell volume. When the volume data are plotted (Figure 2c), it can be seen that the unit cell volume for the front layers of the cell changes nearly linearly during constant current charging with a shallower slope at low states of charge and a higher slope at high states of charge. These two different slopes are attributed to two subtly different structural phases being present at low and high states of charge, each having different sensitivities to the removal of Li ions. This conclusion is consistent with the different voltage profile slopes in these two regimes.

Since the unit cell volume changes monotonically during charge and discharge, it is straightforward to use this volume to

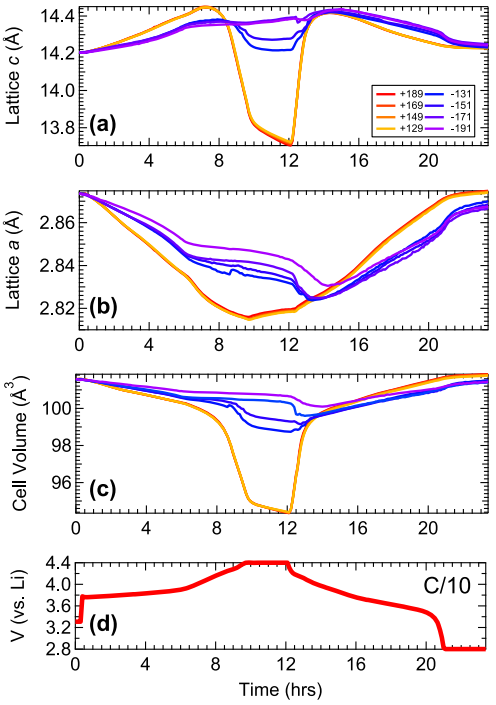

Figure 2. Depth-dependent evolution of (a) *c*-lattice parameter, (b) *a*-lattice parameter, and (c) cell volume during electrochemical cycling at C/10 with (d) the recorded voltage profile. Data from four scans probing the front layers of the cathode closest to the separator (z = +189, +169, +149, and +129 microns) are shown in red→orange, while data from four scans probing the back layers of the electrode closest to the current collector (z = −191, −171, −151, and −131 microns) are shown in purple→blue.

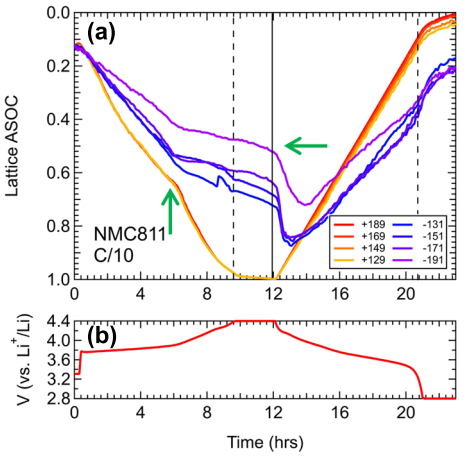

Figure 3. (a) Evolution of ASOC during operando studies of an NMC811 cathode compared for four scans at the front of the cathode (purple→blue) and four scans at the back of the cathode (red→orange), plotted with (b) the voltage profile during cycling. Dashed and solid lines indicate the end of the CC and CV stages during cycling, respectively.

calculate the local state of charge (SOC) at every depth within the cathode at every point during the operando electrochemical cycling of this cell. Instead of calculating the true SOC, which would require complementary operando diffraction data for a thin-film sample that is confirmed to cycle in a completely homogeneous manner, we have instead calculated the relative quantity of an accessible state of charge (ASOC) in which the highest observed volume during cycling is given a value of 0 and the lowest observed volume during cycling is given a value of 1. This calibration was done using the volumetric data collected on the front-most layer of this cell during the first discharge cycle, as described in the Supporting Information (Figure S8). It should be noted that the occurrence of irreversible structural changes during the first cycle results in the lowest volume observed during the first discharge being lower than that of the pristine phase measured before the start of cycling, resulting in the pristine phase having an assigned ASOC of 0.12 rather than the expected value of zero. Moreover, the magnitude of the perturbation due to irreversible structural changes is small relative to the overall magnitude of changes during cycling and thus has a minimal impact on the overall analysis in addition to only affecting the interpretation of the results of the first charge cycle.

The resulting ASOC behavior for the front four and back four layers is plotted in Figure 3. On the whole, the data show that the local state of charge can be probed with a combination of spatial resolution (20 microns), temporal resolution (more than 100 points during each charge and discharge cycle), and high sensitivity (a typical point-to-point scatter of less than 1% in ASOC) in a manner that has not been previously achieved for an industrially relevant thin-film sample. This unprecedented combination of sensitivity and speed allows a number of unusual and unexpected features to be resolved in the data.

The difference in ASOC at different heights within the sample is an expected consequence of the transport limitations that prevent the full capacity of the thick film cathode from being accessed. However, it is unexpected that the difference in ASOC between the front and back of the cathode rapidly accelerates about halfway through the first charge cycle (vertical arrow in Figure 3), a point at which the back of the cell is approximately half-charged and beyond which it does not significantly change its ASOC. This suggests that the mobility limitation has grown to the point at which the back of the cathode is no longer electrochemically active. Curiously, this change is accompanied by acceleration in the rate of charging of the front portion of the cathode, another unexpected feature. It is not yet known if this discontinuous behavior is a consequence of the properties of the material (e.g., change in physical properties resulting in improved transport on crossing a structural phase transition) or a consequence of the inhomogeneous environment of the cell (e.g., large changes in the local electrolyte concentration leading to poor mobility at certain depths).

Second, while the front of the cathode cycles in a manner aligned with the driving potential, the back of the cathode does not. In fact, it can be seen that when the battery cycle switches over from charging to discharging (around 12 h, solid vertical line), the back of the cathode continues to increase its state of charge to up to two additional hours (horizontal arrow in Figure 3) before joining the rest of the cell in discharging. Furthermore, the rate of charging of the back cathode layers during discharge is faster than at any point in the charge cycle. This is especially remarkable since this back portion of the cell stopped actively charging about halfway through the charge cycle, with its ASOC changing by less than 10% in the last 6 h of charging.

The origin of the fast charging behavior during discharge is tentatively attributed to changes in the electrolyte concentration. During charging, the removal of Li^+ ions from the solid ceramic cathode will lead to a transient increase in the local

cathode solution concentration before these ions can diffuse to and deposit on the Li metal anode. When the rate of Li^+ removal is faster relative to the rate of diffusion of the ions in solution, it is expected that the electrolyte solution will be enriched in Li^+ near the cathode and depleted in Li^+ near the anode. These differences are expected to be particularly pronounced far from the anode, namely, at the back layers of the cathode. However, this gradient will be reversed during the discharge process in which the local Li^+ concentrations within the electrolyte in the cathode will be reduced as Li^+ ions in the electrolyte are intercalated into the solid cathode. In this manner, the ability of the front cathode layers to promptly begin intercalating Li^+ ions at the beginning of the discharge cycle may result in a drop in the local Li^+ electrolyte concentrations within the cathode film, thus permitting the accelerated charging of the back cathode layers. These effects may be further amplified by the strongly peaked dependence of Li^+ ion mobility on the solution concentration of Li^+, which in the case of the present EC/DMC electrolyte occurs near a concentration of 1 M.[30]

Fast Cycling. Data were collected for the NMC811 cathode galvanostatically cycled between 2.8 and 4.4 V (vs Li^+/Li) against Li metal at a rate of C/3 (based on a nominal capacity of 200 mAh/g) for 9 total cycles, though with the insertion of an additional 3 cycles carried out at a rate of 1C after the 2nd C/3 cycle. Specific discharge capacities of 40−55 mAh/g were obtained during C/3 cycling, as detailed in Table 1. This corresponds to about a third of the nominal capacity of the cell, resulting in each charge and discharge cycle taking around 1 h. In general, the observed charge capacity was larger than the discharge capacity by about 10 mAh/g and electrochemical behavior that would typically be attributed either to electrolyte decomposition at the cathode (CEI formation) or to self-discharge processes. However, operando diffraction studies of the SOC evolution suggest a different origin of the excess charge capacity.

Table 1. Specific Capacity Charge (Electrochemical) at C/3

	specific capacity (mAh/g)		
cycle #	charge	discharge	excess
1	77	42	25
2	58	51	7
3	60	54	6
4	53	43	10
5[a]	50	48	2
6[a]	58	46	12
7[a]	57	46	11
8[a]	62	51	11
9[a]	58	50	8

[a]Includes capacity from 6 min constant voltage (CV) hold

The time variation of ASOC during fast (C/3) cycling extracted from operando diffraction analyses is shown in Figure 4a for vertical scans with 20 μm steps across a 320 μm total range. Intermediate scans between the highest and the lowest beam vertical position average the response from multiple heights within the thick film due to the relatively large misalignment of the film (~2.4°), and the plotted ASOC was obtained using the weighted average of fits to two-phase Rietveld refinements (different phases for front and back of the cell). During fast cycling, the difference in ASOC between the front and back of the cathode film was very large, with differences up to 0.6 being observed. While the front of the cathode thick film cycles fairly well and reaches an ASOC of 0.8, which is only 20% less than that is seen during cycling at C/10, the back of the thick film (current collector side) is generally insensitive to the changing potential and changes in ASOC by less than 0.1 during cycling. This directly shows that both the driving force for and the timescale of electrochemical processes are very different at different vertical positions within the thick cathode films at high rates.

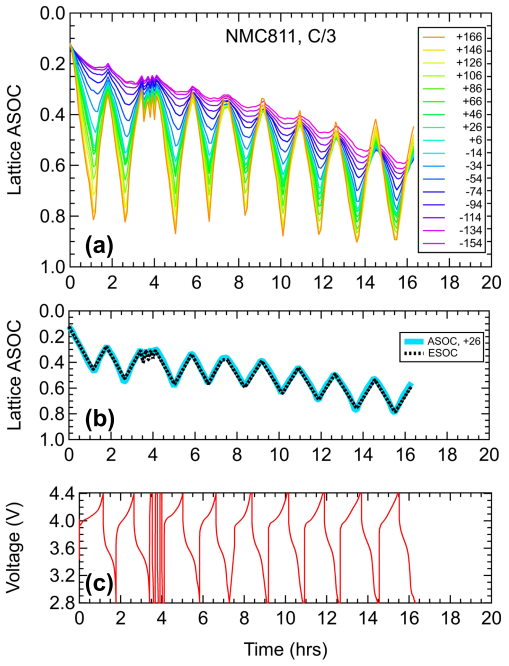

Figure 4. (a) Evolution of the depth-dependent ASOC during operando studies of an NMC811 cathode during fast cycling. (b) Comparison of the accessible SOC (ASOC) calculated from diffraction and the electrochemical SOC (ESOC) calculated from a potentiostat, which was linearly rescaled and offset to match the ASOC scale. (c) Voltage profile during cycling of the NMC811 film.

In addition to capturing the local cathode inhomogeneity, the average response of the cathode can also be extracted from measurements since diffraction scans near the center of the misaligned thick film equally probe all heights of the cathode, as schematically illustrated in Figure S5 (green line). A comparison of the cell-averaged specific state of charge measured from diffraction (ASOC, solid cyan line) and that measured electrochemically using a potentiostat used to cycle the cell (ESOC, dashed black line) is shown in Figure 4b. Remarkably, the results of these two different types of SOC measurements are in nearly perfect agreement, indicating that the excess charge capacity is a real feature of the cathode rather than the signature of a parasitic process.

Based on the operando diffraction data, the origin of the excess capacity can be attributed to the slow timescale of the electrochemical processes near the current collector. Instead of seeing the voltage being applied by the potentiostat at a given point in time, the back layers of the cathode closest to the current collector are expected to experience the time-averaged potential during charge−discharge cycles, which roughly corresponds to the potential needed to drive these layers to a half-charged state. The depth profiling data indeed shows that the ASOC of the back layers increase by about 0.45 over 18 h of fast cycling, indicating a slow evolution to medium

states of charge. As a consequence of the slow increase in the ASOC of the back layers, it can be seen that over time the front cathode layers exhibit both a smaller total change in their ASOC and reach a higher maximum state of ASOC at the end of charging. This indicates a complex interplay of electrochemical processes with different timescales across the different vertical heights of the thick cathode film.

CONCLUSIONS

The excellent spatial and temporal resolution of depth profiling measurements were used to provide unprecedented resolution of electrochemical processes within the thick film cathodes that represent a current frontier in efforts to develop higher energy density rechargeable batteries. Multiple unexpected electrochemical phenomena were resolved through these measurements, including localized charging within a discharging cell, the fastest observed local discharge rates occurring after the end of a discharge cycle, and a gradual increase in the whole-cell state of charge over many hours due to slow local kinetics. Although whole-cell models capable of exactly reproducing the behavior observed during these experiments have not yet been demonstrated, the ability of the operando methods described here to collect state-of-charge data with fine slicing in both space and time will provide the data parameterization required to develop accurate predictive models, which can be used to design advanced battery architectures capable of significantly increasing energy storage densities.

ACKNOWLEDGMENTS

This work was supported by the Assistant Secretary for Energy Efficiency and Renewable Energy, Office of Vehicle Technologies of the U.S. Department of Energy (DOE) through the Advanced Battery Materials Research (BMR) program and the Battery500 Consortium under Contract No. DE-SC0012704. Research was in part carried out at Brookhaven National Laboratory, which is supported by the U.S. Department of Energy, Office of Basic Energy Sciences, under Contract No. DE-SC0012704. The use of the Advanced Photon Source at Argonne National Laboratory was supported by the U. S. Department of Energy, Office of Science, Office of Basic Energy Sciences, under Contract No. DE-AC02-06CH11357.

We gratefully acknowledge the support of the staff at beamlines 11-ID-B (O. Borkiewicz) and 11-BM (S. Lapidus) as well as the use of the dedicated eChem lab facility (K. Wiaderek). We gratefully acknowledge internal discussions with many of our Battery500 Consortium collaborators on experimental and theoretical aspects of depth-dependent measurements, especially Eric Dufek, Y. Shirley Meng, and Michael Toney.

REFERENCES

(1) Whittingham, M. S. Lithium batteries and cathode materials. *Chem. Rev.* **2004**, *104*, 4271−4302.

(2) Wang, Y.; Liu, B.; Li, Q.; Cartmell, S.; Ferrara, S.; Deng, Z. D.; Xiao, J. Lithium and lithium ion batteries for applications in microelectronicdevices: A review. *J. Power Sources* **2015**, *286*, 330−345.
(3) Chu, S.; Majumdar, A. Opportunities and challenges for a sustainableenergy future. *Nature* **2012**, *488*, 294.
(4) Goodenough, J. B.; Park, K.-S. The Li-Ion rechargeablebattery: a perspective. *J. Am. Chem. Soc.* **2013**, *135*, 1167−1176.
(5) Goodenough, J. B. Cathode materials: A personal perspective. *J. Power Sources* **2007**, *174*, 996−1000.
(6) Myung, S.-T.; Maglia, F.; Park, K.-J.; Yoon, C. S.; Lamp, P.; Kim, S.-J.; Sun, Y.-K. Nickel-richlayered cathode materials for automotive Lithium-Ion batteries: achievements and perspectives. *ACS Energy Lett.* **2016**, *2*, 196−223.
(7) Liu, J.; Bao, Z.; Cui, Y.; Dufek, E. J.; Goodenough, J. B.; Khalifah, P.; Li, Q.; Liaw, B. Y.; Liu, P.; Manthiram, A.; Meng, Y. S.; Subramanian, V. R.; Toney, M. F.; Viswanathan, V. V.; Whittingham, M. S.; Xiao, J.; Xu, W.; Yang, J.; Yang, X.-Q.; Zhang, J.-G. Pathways for practical high-energy long-cycling lithium metal batteries. *Nat. Energy* **2019**, *4*, 180−186.
(8) Radin, M. D.; Hy, S.; Sina, M.; Fang, C.; Liu, H.; Vinckeviciute, J.; Zhang, M.; Whittingham, M. S.; Meng, Y. S.; Van der Ven, A. Narrowingthe Gap between Theoretical and Practical Capacities in Li-Ion Layered Oxide Cathode Materials. *Adv. Energy Mater.* **2017**, *7*, 1602888.
(9) Wang, K. X.; Li, X. H.; Chen, J. S. Surface and interface engineering of electrode materials for Lithium-Ion batteries. *Adv. Mater.* **2015**, *27*, 527−545.
(10) Singh, M.; Kaiser, J.; Hahn, H. Thick electrodes for high energy Lithium Ion batteries. *J. Electrochem. Soc.* **2015**, *162*, A1196−A1201.
(11) Singh, M.; Kaiser, J.; Hahn, H. A systematic study of thick electrodes for high energy lithium ion batteries. *J. Electroanal. Chem.* **2016**, *782*, 245−249.
(12) Du, Z.; Wood, D. L.; Daniel, C.; Kalnaus, S.; Li, J. Understanding limiting factors in thick electrode performance as applied to high energy density Li-ion batteries. *J. Appl. Electrochem.* **2017**, *47*, 405−415.
(13) Danner, T.; Singh, M.; Hein, S.; Kaiser, J.; Hahn, H.; Latz, A. Thick electrodes for Li-Ion batteries: A model based analysis. *J. Power Sources* **2016**, *334*, 191−201.
(14) Bak, S.-M.; Shadike, Z.; Lin, R.; Yu, X.; Yang, X.-Q. In situ/operando synchrotron-basedX-ray techniques for lithium-ionbattery research. *NPG Asia Mater.* **2018**, *10*, 563−580.
(15) De Marco, R.; Veder, J.-P. In situ structuralcharacterization of electrochemical systems using synchrotron-radiation techniques. *TrAC, Trends Anal Chem* **2010**, *29*, 528−537.
(16) Borkiewicz, O. J.; Shyam, B.; Wiaderek, K. M.; Kurtz, C.; Chupas, P. J.; Chapman, K. W. The AMPIX electrochemicalcell: a versatile apparatus for in situ X-ray scattering and spectroscopic measurements. *J. Appl. Crystallogr.* **2012**, *45*, 1261−1269.
(17) Morcrette, M.; Chabre, Y.; Vaughan, G.; Amatucci, G.; Leriche, J.-B.; Patoux, S.; Masquelier, C.; Tarascon, J. In situ X-ray diffraction techniques as a powerful tool to study battery electrode materials. *Electrochim. Acta* **2002**, *47*, 3137−3149.
(18) Richard, M.; Koetschau, I.; Dahn, J. A cell for in situ x-ray diffractionbased on coin cell hardwareand Bellcore plastic electrode technology. *J. Electrochem. Soc.* **1997**, *144*, 554−557.
(19) Liu, H.; Allan, P. K.; Borkiewicz, O. J.; Kurtz, C.; Grey, C. P.; Chapman, K. W.; Chupas, P. J. A radiallyaccessible tubular in situ X-ray cell for spatially resolved operando scattering and spectroscopic studies of electrochemicalenergy storage devices. *J. Appl. Crystallogr.* **2016**, *49*, 1665−1673.
(20) Liu, H.; Kazemiabnavi, S.; Grenier, A.; Vaughan, G.; Di Michiel, M.; Polzin, B. J.; Thornton, K.; Chapman, K. W.; Chupas, P. J. Quantifyingreaction and rate heterogeneityin battery electrodes in 3D through operando X-ray diffraction computed tomography. *ACS Appl. Mater. Interfaces* **2019**, *11*, 18386−18394.
(21) Chen, S.; Niu, C.; Lee, H.; Li, Q.; Yu, L.; Xu, W.; Zhang, J.-G.; Dufek, E. J.; Whittingham, M. S.; Meng, S. Critical parameters for evaluating coin cells and pouch cells of rechargeable Li-metal batteries. *Joule* **2019**, *3*, 1094−1105.
(22) Son, I. H.; Park, J. H.; Park, S.; Park, K.; Han, S.; Shin, J.; Doo, S. G.; Hwang, Y.; Chang, H.; Choi, J. W. Graphene balls for lithium rechargeable batteries with fast charging and high volumetricenergy densities. *Nat. Commun.* **2017**, *8*, 1−11.
(23) Toby, B. H.; Von Dreele, R. B. GSAS-II: the genesis of a modern open-sourceall purpose crystallographysoftware package. *J. Appl. Crystallogr.* **2013**, *46*, 544−549.
(24) Liu, H.; Li, Z.; Grenier, A.; Kamm, G. E.; Yin, L.; Mattei, G. S.; Cosby, M. R.; Khalifah, P. G.; Chupas, P. J.; Chapman, K. W. Best practices for operando depth-resolvingbattery experiments. *J. Appl. Crystallogr.* **2020**, *53*, 133−139.
(25) Wang, J.; Toby, B. H.; Lee, P. L.; Ribaud, L.; Antao, S. M.; Kurtz, C.; Ramanathan, M.; Von Dreele, R. B.; Beno, M. A. A dedicated powder diffraction beamline at the advanced photon source: commissioningand early operationalresults. *Rev. Sci. Instrum.* **2008**, *79*, No. 085105.
(26) Li, W.; Asl, H. Y.; Xie, Q.; Manthiram, A. Collapse of $LiNi_{1-x-y}Co_xMn_yO_2$ Lattice at Deep Charge Irrespective of Nickel Content in Lithium-IonBatteries. *J. Am. Chem. Soc.* **2019**, *141*, 5097−5101.
(27) Märker, K.; Reeves, P. J.; Xu, C.; Griffith, K. J.; Grey, C. P. Evolution of structure and lithium dynamics in $LiNi_{0.8}Mn_{0.1}Co_{0.1}O_2$ (NMC811) cathodes during electrochemical cycling. *Chem. Mater.* **2019**, *31*, 2545−2554.
(28) Ryu, H.-H.; Park, K.-J.; Yoon, C. S.; Sun, Y.-K. Capacity Fading of Ni-Rich $Li[Ni_xCo_yMn_{1-x-y}]O_2$ ($0.6 \leq x \leq 0.95$) Cathodes for High-Energy-DensityLithium-IonBatteries: Bulk or Surface Degradation? *Chem. Mater.* **2018**, *30*, 1155−1163.
(29) Li, J.; Downie, L. E.; Ma, L.; Qiu, W.; Dahn, J. Study of the failure mechanisms of $LiNi_{0.8}Mn_{0.1}Co_{0.1}O_2$ cathode material for lithium ion batteries. *J. Electrochem. Soc.* **2015**, *162*, A1401−A1408.
(30) Xu, K. Electrolytes and interphases in Li-ion batteries and beyond. *Chem. Rev.* **2014**, *114*, 11503−11618.